Electrical conductivity of quark matter at finite *T* under external magnetic field

Seung-il Nam[*]

School of Physics, Korea Institute for Advanced Study (KIAS), Seoul 130-722, Republic of Korea
(Received 17 July 2012; published 29 August 2012)

We investigate the electrical conductivity (σ) of quark matter via the Kubo formula at finite temperature and zero quark density ($T \neq 0$, $\mu = 0$) in the presence of an external strong magnetic field. For this purpose, we employ the dilute instanton-liquid model, taking into account its temperature modification with the trivial-holonomy caloron distribution. By doing that, the momentum and temperature dependences for the effective quark mass and model renormalization scale are carefully evaluated. From the numerical results, it turns out that $\sigma \approx (0.02$–$0.15)$ fm^{-1} for $T = (0$–$400)$ MeV with the relaxation time $\tau = (0.3$–$0.9)$ fm. In addition, we also parametrize the electrical conductivity as $\sigma/T \approx (0.46, 0.77, 1.08, 1.39)C_{\mathrm{EM}}$ for $\tau = (0.3, 0.5, 0.7, 0.9)$ fm, respectively. These results are compatible with other theoretical estimations, including those from the lattice QCD simulations. It also turns out that the external magnetic field plays only a minor role for σ even for the very strong one $B_0 \sim m_\pi^2 \times 10$ and becomes relatively effective for $T \lesssim 200$ MeV. Moreover, we compute the soft photon emission rate from the quark-gluon plasma, using the electrical conductivity calculated.

I. INTRODUCTION

QCD at extreme conditions has been one of the most celebrated subjects in high-energy physics for decades. The observation of the strong magnetic field $B_0 \sim m_\pi^2$ in the noncentral heavy-ion collision at the Relativistic Heavy Ion Collider (RHIC) of Brookhaven National Laboratory [1–4] triggered abundant research works, such as the chiral magnetic effect (CME) [5–8], chiral magnetic wave [9,10], QCD phase structure in the presence of magnetic fields, related to the magnetic catalysis [11–13], and electromagnetic properties of QCD matter [14–19]. In addition to the magnetic field, the transport coefficients for the hot and/or dense matter is of great importance in general as well, since they characterize the physical properties of the matter. In general, those coefficients can be studied by the Kubo formula [20–22]. Among them, in the present work, we want to investigate the electrical conductivity (σ), which corresponds to the vector-current correlation (VCC) and its spectral functions [18], for quark matter at finite temperature and zero quark density ($T \neq 0$, $\mu = 0$). This condition resembles the present heavy-ion collision experimental conditions, such as RHIC and Large Hadron Collider of CERN, in the presence of the external magnetic field. We note that the conductivity affects much on the magnetic field in terms of the relaxation time [14,19]. The spectral functions are deeply related to the thermal dilepton production, and the production cross section contains much information on the hadron properties, produced in quark-gluon plasma (QGP) [23].

The electrical conductivity was investigated in the hot phase of the QCD plasma and extracted from a quenched SU

(3) lattice QCD (LQCD) simulation of the Euclidean time VCC for $1.5 \leq T/T_c \leq 3$, resulting in $\sigma/T \approx 7C_{\mathrm{EM}}$, where $C_{\mathrm{EM}} = \sum_f e_f^2$ and e_f denotes the electric charge for the quark with a flavor f, in Ref. [22]. Similarly, the electrical conductivity was studied with quenched SU(3) LQCD with the maximum entropy method for VCC in the deconfined phase $T \sim 1.45T_c$ in Ref. [18], in which the dilepton production rate was studied as well. In that work, the electrical conductivity turned out to be $1/3 \lesssim \sigma/(C_{\mathrm{EM}}T) \lesssim 1$. Note that the estimated value for σ is about one order larger in Ref. [22] in comparison to those from Ref. [18]. In Ref. [19], VCC in quenched SU(2) LQCD simulation was investigated with a chirally invariant lattice Dirac operator with a constant external magnetic field. It was observed that $\sigma_\perp$ and $\sigma_\parallel$, which are perpendicular and parallel to the external magnetic field, respectively, are almost the same and insensitive to the external magnetic field for $T \gtrsim T_c$, whereas there appear considerable differences between them at $T \sim 0$ with respect to the magnetic field. The electrical conductivity was also estimated as $\sigma_\perp \approx \sigma_\parallel \approx \sigma = (0.076 \pm 0.010)$ fm^{-1} for $T \approx 350$ MeV with $T = 1.12T_c$. Beside the LQCD simulations, using the Green-function method, the electrical conductivity was explored at finite T and μ: $T \approx 100$ MeV and $\mu \approx 400$ MeV [14]. At specific choices for the model parameters, the electrical conductivity resulted in $\sigma \approx 0.04$ fm^{-1}, which is similar to those from Refs. [18,19]. Interestingly, they found that the electrical conductivity is very insensitive to the external magnetic field.

Considering the rather unsettled situation for the electrical conductivity for hot and dense quark matter as mentioned above, in the present work, we employ the dilute instanton-liquid model to study it [24,25]. The model is characterized by the two phenomenological (instanton) parameters: average inter-(anti)instanton distance

*sinam@kias.re.kr

$\bar{R} \approx 1$ fm and (anti)instanton size $\bar{\rho} \approx 1/3$ fm. In the instanton ensemble, representing the nonperturbative QCD vacuum, the quarks are delocalized by flipping their helicities. As a result, the quarks acquire their momentum-dependent effective mass, corresponding to the finite value for the chiral condensate and manifesting the spontaneous breakdown of chiral symmetry (SBCS). Moreover, the momentum-dependent quark mass plays the role of a UV regulator by construction. Since we are interested in the case at finite T, the caloron with trivial holonomy is used to modify the instanton parameters [26,27]. By doing that, the instanton size $\bar{\rho}$ becomes a smoothly decreasing function of T, signaling weakening nonperturbative effects of QCD. In addition, we utilize the fermionic Matsubara formula for inclusion of T in the relevant physical quantities in hand. To take into account the external magnetic field, which is produced in the peripheral heavy-ion collisions, the Schwinger method is employed [28–30].

Using the Kubo formula for the electrical conductivity, we compute σ as a function of T and the relaxation time τ for the SU(2) light-flavor sector in the chiral limit, i.e., $m_u \sim m_d \sim 0$. From the numerical results, it turns out that $\sigma \approx (0.02–0.15)$ fm^{-1} for $T = (0–400)$ MeV with the relaxation time $\tau = (0.3–0.9)$ fm. In addition, we also parametrize the electrical conductivity as $\sigma/T \approx (0.46, 0.77, 1.08, 1.39)C_{EM}$ for $\tau = (0.3, 0.5, 0.7, 0.9)$ fm, respectively. These results are compatible with other theoretical estimations, including those from the lattice QCD simulations. It also turns out that the external magnetic field plays only a minor role for σ even for the very strong magnetic field $B_0 \approx m_\pi^2 \times 10$ and becomes relatively effective for $T \lesssim 200$ MeV. Moreover, we also compute the soft photon emission rate from the quark-gluon plasma, using the electrical conductivity calculated.

The present work is organized as follows: In Sec. II, we briefly introduce the present theoretical framework. The numerical results and related discussions are given in Sec. III. The last section is devoted to the summary, conclusion, and future perspectives.

II. THEORETICAL FRAMEWORK

Now, we make a brief explanation for the theoretical framework for computing the electrical conductivity. We note that all the calculations are performed in flavor SU(2) in the chiral limit $(m_u, m_d) \to 0$. First, the electrical conductivity can be defined in Euclidean space from the Kubo formula as follows [14]:

$$\sigma_{\mu\nu}(p) = -\sum_f \frac{e_f^2}{w_p} \int \frac{d^4k}{(2\pi)^4} \mathrm{Tr}_{c,\gamma}[S(k)\gamma_\mu S(k+p)\gamma_\nu]_A. \quad (1)$$

Here, e_f stands for the electrical charge for a light-flavor (f) quark, i.e., $(e_u, e_d) = (2e/3, -e/3)$, where e denotes the unit charge $\sqrt{4\pi\alpha_{EM}}$ with the fine structure constant $\alpha_{EM} \approx 1/137$. w_p indicates the Matsubara frequency for

the momentum p for σ, being proportional to $2\pi T$. $\mathrm{Tr}_{c,\gamma}$ is assigned as the trace over the color and Lorentz indices. The subscript A at $[\cdots]_A$ means that we have introduced the externally induced electromagnetic (EM) vector field A_μ. Note that, in Eq. (1), we have taken into account only the connected-diagram contribution, since the disconnected-diagram one $\propto (e_u + e_d)^2$ contributes to the electrical conductivity negligibly [18]. The longitudinal and transverse components for the electrical conductivity are defined with Eq. (1) as

$$\sigma_\perp \equiv \lim_{w_p \to 0} \lim_{\boldsymbol{p} \to 0}[\sigma_{11,22}(p)], \quad \sigma_\parallel \equiv \lim_{w_p \to 0} \lim_{\boldsymbol{p} \to 0}[\sigma_{33}(p)]. \quad (2)$$

To evaluate Eq. (1), we make use of the dilute instanton-liquid model [24,25]. This model is based on the idea that the quarks interact with the nontrivial QCD-vacuum configuration, i.e., instanton ensemble, by flipping their chiralities. As a result, the quark acquires the dynamically generated effective mass, and SBCS is explained. The model is also characterized by the two phenomenological parameters for the light-flavor sectors: average inter-(anti)instanton distance $\bar{R}$ and average (anti)instanton size $\bar{\rho}$. For vacuum, these values are phenomenologically chosen to be $(\bar{R}, \bar{\rho}) \approx (1, 1/3)$ fm [24,25]. In Euclidean space, the effective chiral action (EChA) of the model reads

$$\mathcal{S}_{eff} = -\mathrm{Sp}_{c,f,\gamma}\ln[i\slashed{\partial} - iM(D^2)], \quad (3)$$

where $\mathrm{Sp}_{c,f,\gamma}$ stands for the functional trace over the color, flavor, and Lorentz indices, while $M(D^2)$ stands for the momentum-dependent effective quark mass from the quark zero-mode solution in the instanton vacuum [25]. Note that D indicates the U(1) covariant derivative $iD_\mu = i\partial_\mu + e_f A_\mu$. In this way, we induce the external EM field to EChA: the Schwinger method [28–30]. From EChA, one can derive the light-quark propagator under the external EM field in the momentum space as [31]

$$S(K) = \frac{\slashed{K} + iM_K^2}{K^2 + M_K^2} \approx \frac{\slashed{K} + i[M_k + \frac{1}{2}\tilde{M}_k(\sigma \cdot F)]}{k^2 + M_k^2}. \quad (4)$$

Here, $K_\mu \equiv k_\mu + e_f A_\mu$ and $\sigma \cdot F \equiv \sigma_{\mu\nu}F^{\mu\nu}$. $F^{\mu\nu}$ stands for the photon field strength tensor. The effective quark mass and its derivative $\tilde{M}_k$ in Eq. (4) are defined by [31]

$$M_k = M_0\left[\frac{2}{2 + \bar{\rho}^2 k^2}\right]^2, \quad \tilde{M}_k = -\frac{8M_0\bar{\rho}^2}{(2 + \bar{\rho}^2 k^2)^3}, \quad (5)$$

where M_0 and $\bar{\rho}$ denote constituent-quark mass at zero virtuality and average (anti)instanton size, respectively. From Ref. [32], M_0 is determined as about 350 MeV for $1/\bar{\rho} \approx 600$ MeV to reproduce the pion weak-decay constant F_π.

Now, we want to explain briefly how to modify $\bar{\rho}$ and M_0 as a function of T, using the caloron solution. Details can be found in Ref. [27]. An instanton distribution function for arbitrary N_c and N_f can be written with a Gaussian

suppression factor as a function of T and an arbitrary instanton size ρ for pure-glue QCD [26]:

$$d(\rho, T) = \underbrace{C_{N_c} \Lambda_{\mathrm{RS}}^b \hat{\beta}^{N_c}}_{c} \rho^{b-5} \exp[-(A_{N_c} T^2 + \bar{\beta}\gamma n \bar{\rho}^2)\rho^2].$$

(6)

We note that the *CP*-invariant vacuum was taken into account in Eq. (6), and we assumed the same analytical form of the distribution function for both the instanton and the anti-instanton. Note that the instanton packing fraction $n \equiv 1/\bar{R}^4$ and $\bar{\rho}$ have been taken into account as functions of T implicitly. We also assigned the constant factor in the right-hand side of the above equation as $\mathcal{C}$ for simplicity. The abbreviated notations are also given as

$$\hat{\beta} = -b\ln[\Lambda_{\mathrm{RS}}\rho_{\mathrm{cut}}], \qquad \bar{\beta} = -b\ln[\Lambda_{\mathrm{RS}}\langle R \rangle],$$

$$C_{N_c} = \frac{4.60 e^{-1.68\alpha_{\mathrm{RS}} N_c}}{\pi^2 (N_c - 2)!(N_c - 1)!}, \qquad A_{N_c} = \frac{1}{3}\left[\frac{11}{6}N_c - 1\right]\pi^2,$$

$$\gamma = \frac{27}{4}\left[\frac{N_c}{N_c^2 - 1}\right]\pi^2, \qquad b = \frac{11N_c - 2N_f}{3}.$$

(7)

Note that we defined the one-loop inverse charges $\hat{\beta}$ and $\bar{\beta}$ at certain phenomenological cutoff ρ_{cut} and $\langle R \rangle \approx \bar{R}$. Λ_{RS} denotes a scale, depending on a renormalization scheme, whereas V_3 is for the three-dimensional volume. Using the instanton distribution function in Eq. (6), we can compute the average value of the instanton size $\bar{\rho}^2$ straightforwardly as follows [33]:

$$\bar{\rho}^2(T) = \frac{\int d\rho \rho^2 d(\rho, T)}{\int d\rho d(\rho, T)} = \frac{[A_{N_c}^2 T^4 + 4\nu\bar{\beta}\gamma n]^{\frac{1}{2}} - A_{N_c} T^2}{2\bar{\beta}\gamma n},$$

(8)

where $\nu = (b - 4)/2$. It can easily be shown that Eq. (8) satisfies the following asymptotic behaviors [33]:

$$\lim_{T \to 0}\bar{\rho}^2(T) = \sqrt{\frac{\nu}{\bar{\beta}\gamma n}}, \qquad \lim_{T \to \infty}\bar{\rho}^2(T) = \frac{\nu}{A_{N_c} T^2}.$$

(9)

Here, the second relation of Eq. (9) indicates a correct scale-temperature behavior at high T, i.e., $1/\bar{\rho} \approx \Lambda \propto T$. Substituting Eq. (8) into Eq. (6), the caloron distribution function can be evaluated further:

$$d(\rho, T) = \mathcal{C}\rho^{b-5} \exp[-\mathcal{F}(T)\rho^2],$$
$$\mathcal{F}(T) = \frac{1}{2}A_{N_c} T^2 + \left[\frac{1}{4}A_{N_c}^2 T^4 + \nu\bar{\beta}\gamma n\right]^{1/2}.$$

(10)

The instanton packing fraction n can be computed self-consistently, using the following equation:

$$n^{\frac{1}{\nu}}\mathcal{F}(T) = [\mathcal{C}\Gamma(\nu)]^{\frac{1}{\nu}},$$

(11)

where we replaced $NT/V_3 \to n$, and $\Gamma(\nu)$ stands for the Γ function with an argument ν. Note that $\mathcal{C}$ and $\bar{\beta}$ can be determined easily using Eqs. (8) and (12), incorporating the vacuum values for $n \approx (200\ \mathrm{MeV})^4$ and $\bar{\rho} \approx (600\ \mathrm{MeV})^{-1}$: $\mathcal{C} \approx 9.81 \times 10^{-4}$ and $\bar{\beta} \approx 9.19$. Finally, for estimating the T dependence of M_0, one needs to consider the normalized distribution function, defined as follows:

$$d_N(\rho, T) = \frac{d(\rho, T)}{\int d\rho d(\rho, T)} = \frac{\rho^{b-5}\mathcal{F}^\nu(T) \exp[-\mathcal{F}(T)\rho^2]}{\Gamma(\nu)}.$$

(12)

Here, the subscript N denotes the normalized distribution. For brevity, we want to employ the large-N_c limit to simplify the expression for $d_N(\rho, T)$. In this limit, as understood from Eq. (12), $d_N(\rho, T)$ can be approximated as a δ-function:

$$\lim_{N_c \to \infty} d_N(\rho, T) = \delta[\rho - \bar{\rho}(T)].$$

(13)

The trajectory of this δ function projected on the ρ-T plane is depicted in the left panel of Fig. 1 by the thick-solid line.
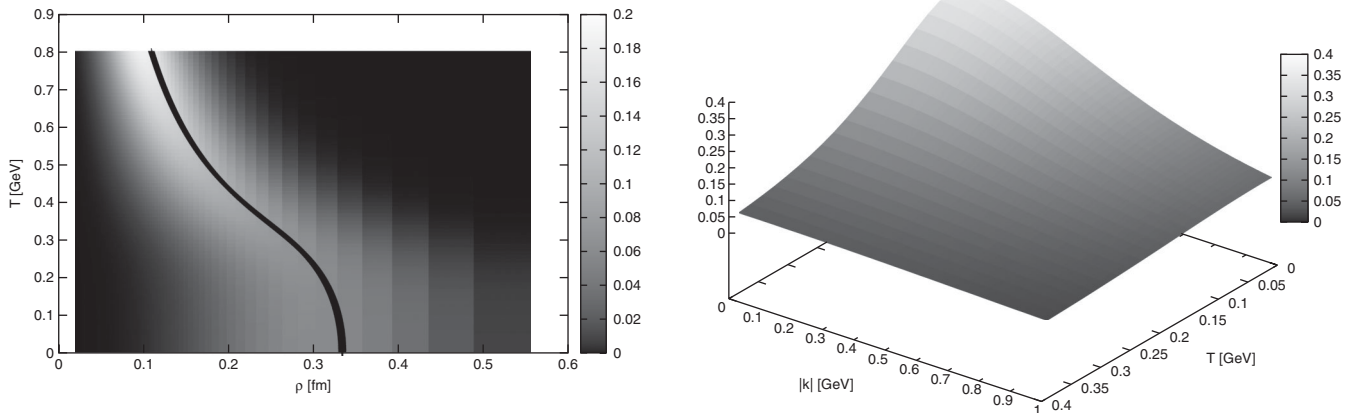

FIG. 1. Left: $d_N(\rho, T)$ on the ρ-T plane. The trajectory on the curve represents $\bar{\rho}(T)$ in Eq. (8). Right: Momentum-temperature dependent effective quark mass in Eq. (14).

Using Eq. (13), we can write finally the $(|k|, T)$-dependent M as follows:

$$M_k = M_0 \left[\frac{\sqrt{n(T)}\bar{\rho}^2(T)}{\sqrt{n(0)}\bar{\rho}^2(0)} \right] \left[\frac{2}{2 + k^2 \bar{\rho}^2(T)} \right]^2, \quad (14)$$

where we used $M_0 \approx 350$ MeV at $T \rightarrow 0$. Note that $\bar{\rho}$ and n are functions of T in Eq. (14). We show the momentum-temperature dependent effective quark mass in Eq. (14) in the right panel of Fig. 1. As shown there, the effective quark mass is a smoothly decreasing function of momentum as well as temperature as expected.

Considering all the ingredients discussed above and plugging Eq. (4) into Eq. (1), we obtain the following expression for the transverse components of σ with $(\mu, \nu) = (1, 1)$ or (2,2) and $F_{12} = B_0$ in the z direction:

$$\sigma_{\mu\nu}(p) = \sum_f \frac{4e_f^2 N_c \delta_{\mu\nu}}{w_p}$$
$$\times \int \frac{d^4 k}{(2\pi)^4} \left[\frac{\frac{k(k+p)}{2} + M_k^2 - 2\tilde{M}_k^2(e_f B_0)^2}{[k^2 + M_k^2][(k+p)^2 + M_k^2]} \right]. \quad (15)$$

For the longitudinal one $(\mu, \nu) = (3, 3)$, one removes the term proportional to B_0^2 in Eq. (15). Since we are interested in the finite T case, we introduce the fermionic Matsubara formula for Eq. (15) and then have the following expression:

$$\sigma_{\mu\nu}(p) = \sum_f \frac{8e_f^2 N_c T \delta_{\mu\nu}}{w_p} \sum_n \int \frac{d^3 k}{(2\pi)^3}$$
$$\times \left[\frac{\frac{k^2 + w_k(w_k + w_p)}{2} + M_k^2 - 2\tilde{M}_k^2(e_f B_0)^2}{[k^2 + w_k^2 + M_k^2][k^2 + (w_k + w_p)^2 + M_k^2]} \right]. \quad (16)$$

Here, $n \geq 0$ for representing the retarded Green function. For definiteness, we made use of $p = (\vec{0}, w_p)$ in deriving Eq. (16). Note that we have simplified the mass functions in Eq. (17) by replacing the four momentum into three momentum, $k \rightarrow \boldsymbol{k}$, in comparison to Eq. (15):

$$M_{\boldsymbol{k}} \approx M_0(T) F_{\boldsymbol{k}}^2, \quad F_{\boldsymbol{k}} = \frac{2}{2 + \bar{\rho}^2(T)\boldsymbol{k}^2},$$
$$\tilde{M}_{\boldsymbol{k}} \approx -\frac{8M_0(T)\bar{\rho}^2(T)}{[2 + \bar{\rho}^2(T)k^2]^3}, \quad (17)$$

where $M_0(T)$ and $\bar{\rho}(T)$ are given in Eqs. (14) and (13). We verified that this simplification does not make considerable changes in the numerical results but does make the analytical and numerical calculations much easier. Note that the fermionic Matsubara frequency for the loop w_k is defined with the finite relaxation time τ for computing the finite electrical conductivity as in Ref. [14]:

$$w_k = w_n \left(1 + \frac{1}{2\tau|w_n|} \right). \quad (18)$$

Here, $w_n = (2n + 1)\pi T$ and $n \in \mathcal{I}$. We want to make an assumption: It is clear that the term $1/(2|w_n|)$ in Eq. (18) becomes its maximum and most effective when $n = 0$. Hence, it is reasonable to replace $|w_n| \rightarrow |w_0| = \pi T$ in the parentheses in the right-hand side of Eq. (18). Moreover, if we consider $w_p \approx 2\pi T$, w_k in Eq. (18) can be simplified further as follows:

$$w_n \left(1 + \frac{1}{2\pi T\tau} \right) \approx w_n \left(1 + \frac{1}{w_p\tau} \right). \quad (19)$$

In what follows, we will use Eq. (19) rather than Eq. (18) for the Matsubara frequency in the calculations.

The summations over n in Eq. (16) can be developed neatly as follows:

$$\sum_n \frac{T}{[\eta^2 w_n^2 + E_k^2]} = \frac{1}{4\eta E_k} \tanh\left(\frac{E_k}{2\eta T} \right),$$
$$\sum_n \frac{T}{[\eta^2 w_n^2 + E_k^2]^2} = \frac{1}{16\eta^2 T E_k^3} \text{sech}^2\left(\frac{E_k}{2\eta T} \right)$$
$$\times \left[\eta T \sinh\left(\frac{E_k}{\eta T} \right) - E_k \right], \quad (20)$$

where we have defined a notation as $\eta \equiv 1 + 1/(w_p\tau)$. Combining Eqs. (2), (19), and (20) we have the following final expression for σ for $w_p \rightarrow 0$:

$$\sigma_\perp = \sum_f e_f^2 N_c \tau \left\{ \int \frac{d^3 \boldsymbol{k}}{(2\pi)^3} F_{\boldsymbol{k}}^2(k^2) \left[\frac{\tanh(\pi\tau E_k)}{E_k} \right] \right.$$
$$+ \frac{\tau\pi}{2} \int \frac{d^3 \boldsymbol{k}}{(2\pi)^3} F_{\boldsymbol{k}}^2(k^2)$$
$$\times \left[\frac{\text{sech}^2(\pi\tau E_k)}{E_{\boldsymbol{k}}^3} \left[\frac{\sinh(2\pi\tau E_k)}{2\pi\tau} - E_k \right] \right]$$
$$\times [M_{\boldsymbol{k}}^2 - 4\tilde{M}_{\boldsymbol{k}}^2(e_f B_0)^2] \left. \right\}. \quad (21)$$

The energy of the quark is given by $E_k = (k^2 + M_{\boldsymbol{k}}^2)^{1/2}$. We note that we inserted $F_{\boldsymbol{k}}^2(k^2)$ in the integrals in Eq. (21) to tame the UV divergence smoothly in integrating over $\boldsymbol{k}$, instead of setting a three-dimensional cutoff. $\sigma_\parallel$ can be easily obtained by putting $B_0 = 0$ in Eq. (21).

Finally in this section, we want to discuss briefly the chiral phase transition of the present model. One can explore the chiral structure via the chiral (quark) condensate $\langle \bar{q}q \rangle$ within the present model [27,34]:

$$\langle \bar{q}q \rangle = -N_c N_f \int \frac{d^3 \boldsymbol{k}}{(2\pi)^3} \frac{M_{\boldsymbol{k}}^2}{E_k} \left[\frac{1 - \exp(-\frac{3E_k}{T})}{1 + \exp(-\frac{3E_k}{T})} \right]. \quad (22)$$

From the numerical results given in Ref. [34], the chiral condensate turns out to be a smoothly decreasing function of T, which is rather different from the universal class pattern of the chiral phase transition; i.e., there appears
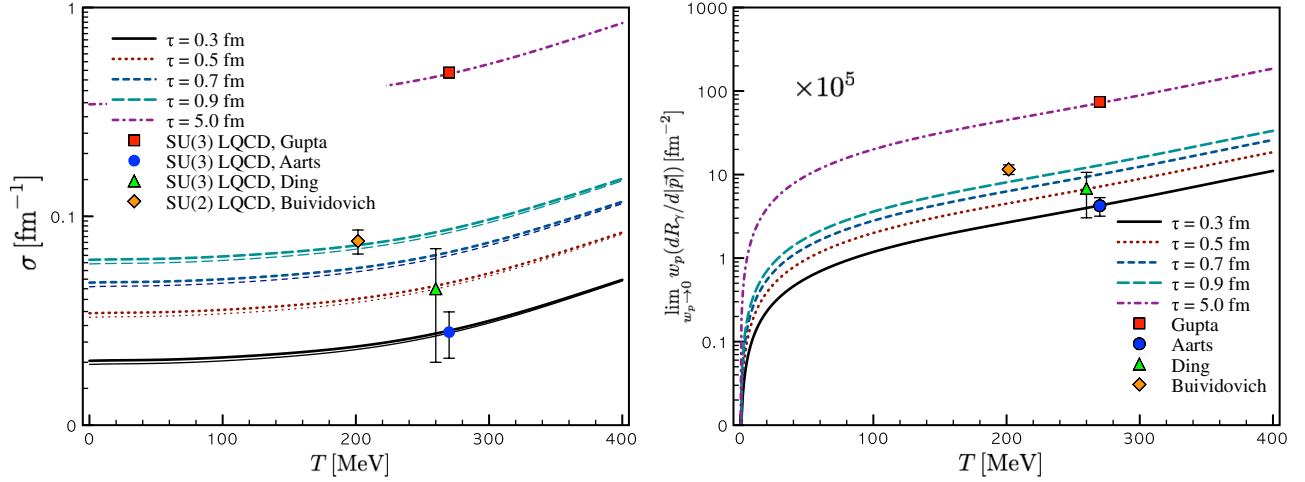
FIG. 2 (color online).   Left: electrical conductivity σ as functions of temperature T for different relaxation times $\tau = (0.3–0.9)$ fm. The thick line indicates the case with $B_0 = 0(\sigma_\parallel)$, whereas the thin ones for $B_0 = m_\pi^2 \times 10(\sigma_\perp)$, in Eq. (21). SU($N_c$) LQCD estimations are taken from Gupta [22], Aarts *et al.* [42], Ding *et al.* [18], and Buividovich *et al.* [19]. Right: Soft photon emission rate in Eq. (24), $\mathcal{R}_\gamma$ in Eq. (24) as functions of T for different τ's in the same manner with the left panel. For all the curves in the left and right panels, we have chosen $T_c \approx 180$ MeV as a trial.

the second-order phase transition for the SU(2) light-flavor sector in the chiral limit $m_q \to 0$. We note that, if the meson-loop correction (MLC), which relates to the $1/N_c$ correction, is taken into account, the correct second-order phase transition was observed for the vanishing current-quark mass, giving $T_c \approx 160$ MeV [34]. Since we have not taken into account the MLC contribution in the present work, the chiral phase transition structure of the present theoretical framework is distinctive from that of the reality so that the inclusion of MLC can change the numerical results for σ to a certain extent. We, however, note that the MLC contribution is ineffective for VCC $\sim \langle J_\mu J_\nu \rangle$ in the chiral limit in general [35]. Hence, it is rather safe to ignore the MLC contribution for the electrical conductivity as in the present work, despite the problematic issue on the chiral structure at finite T as discussed above. We would like to leave this interesting task for the inclusion of the MLC contribution for the future.

III. NUMERICAL RESULTS AND DISCUSSIONS

In this section, we present the numerical results for σ and make comparisons with other theoretical results mainly from the LQCD simulation data. In the left panel

of Fig. 2, we show the numerical results of $\sigma_\perp$ (thick) and $\sigma_\parallel$ (thin) for different τ values, $\tau = (0.1, 0.3, 0.5, 0.9)$ fm in (solid, dotted, dashed, dot-dashed) lines, respectively, as functions of T. As for the external magnetic field, we set it to be $B_0 = m_\pi^2 \times 10$ as a trial. Note that this value of B_0 is still far stronger than that observed in the RHIC experiment [1–4]. From the figure, it turns out that σ is a rapidly increasing function of T and shows the obvious increases beyond $T \approx 200$ MeV. By comparing those cases with and without B_0, we also find that the effect from the external magnetic field is considerably small and only relatively effective in the low-T region $T \lesssim 200$ MeV. Hence, we can conclude from the present model that $\sigma_\perp \approx \sigma_\parallel \equiv \sigma$. For reference, we list σ values for some typical temperatures in Table I, in which one can easily see that σ is almost linear for $T \lesssim 150$ MeV and increases monotonically after that temperature. For instance, at $T_c \approx 180$ MeV, which is close to the transition temperature of QCD, calculated from the full LQCD simulations [36,37], we have $\sigma = (0.023, 0.039, 0.054, 0.070)$ fm^{-1} for $\tau = (0.1, 0.3, 0.5, 0.9)$ fm. It is worth mentioning that, in the recent LQCD simulations [38–41], the transition temperature was obtained as $T_c \approx 155$ MeV, which is lower than those from Refs. [36,37]. At $T_c \approx 155$ MeV, for

TABLE I.   Typical values of σ in Eq. (23) [fm^{-1}] at $B_0 = 0$ for different T and τ values.

	$T = 0$	$T = 100$ MeV	$T = 200$ MeV	$T = 300$ MeV	$T = 400$ MeV
$\tau = 0.3$ fm	0.020	0.021	0.024	0.031	0.049
$\tau = 0.5$ fm	0.034	0.036	0.040	0.053	0.083
$\tau = 0.7$ fm	0.048	0.050	0.056	0.074	0.116
$\tau = 0.9$ fm	0.062	0.064	0.072	0.095	0.149

instance, we have $\sigma = (0.022, 0.037, 0.052, 0.067)$ fm^{-1} for $\tau = (0.1, 0.3, 0.5, 0.9)$ fm. Hence, we conclude that there is only a small change in σ ($\sim$ a few percent) for different T_c values below 200 MeV as shown in the left panel of Fig. 2.

For practical applications as in the LQCD simulations [22,42], it is quite convenient to parametrize the present numerical results for σ as follows:

$$\sigma(T) = C_{\text{EM}} \sum_{m=1} \mathcal{C}_m T^m, \qquad \frac{\mathcal{C}_m}{\text{fm}^{m-1}} \in \mathcal{R}. \qquad (23)$$

Here, we define $C_{\text{EM}} = \sum_f e_f^2 \approx 0.051$ for the SU(2) light-flavor sector. Obtained coefficients up to $m = 3$ are given in Table II. As shown in the coefficients, the electrical conductivity can be parametrized almost linearly with respect to T, i.e., $|\mathcal{C}_{2,3}| \sim 0$. Hence, we can approximate them as $\sigma/T \approx (0.46, 0.77, 1.08, 1.39) C_{\text{EM}}$ for $\tau = (0.3, 0.5, 0.7, 0.9)$ fm, respectively.

In Refs. [22,42], employing the SU(3) quenched LQCD simulations, it was estimated that $\sigma/T = 7 C_{\text{EM}}$ for $1.5 < T/T_c < 3$ and $\sigma/T = (0.4 \pm 0.1) C_{\text{EM}}$ for $T/T_c \approx 1.5$, respectively. Note that there is one order difference between these σ values, although the temperature ranges are not overlapped. In the left panel of Fig. 2, we depict these two LQCD values from Ref. [22] (square) and Ref. [42] (circle), using $T_c \approx 180$ MeV as a trial, although the transition temperatures are slightly higher than this value in general in the quenched LQCD simulations. It is shown that the data point from Ref. [42] is consistent with our numerical result for $\tau \approx 0.3$ fm. On the contrary, the data point from Ref. [22] for $T = 270$ MeV is much larger than ours for $\tau = (0.3 - 0.9)$ fm. We verified that, in order to reproduce it, τ becomes about 5 fm in our model calculation as shown in the left panel of Fig. 2 in the dot-dashed line. In Ref. [43], the characteristic τ was estimated using Ref. [22], resulting in about $(2.2T/T_c)$ fm with a conservative estimate of the QGP medium size. Taking $T \approx 270$ MeV $= T_c \times 1.5$ MeV, it is given that $\tau \approx 5$ fm, which is consistent with our model estimation as shown in the left panel of Fig. 2. Similarly, at $T \approx 1.45 T_c$, it was suggested that $\sigma/T \approx (1/3 - 1) C_{\text{EM}}$ in Ref. [18]. If we choose $T_c \approx 180$ MeV again, this result provides that $\sigma = (0.022 - 0.067)$ fm^{-1}, which is drawn in the left panel of Fig. 2 (triangle), and it corresponds to $\tau \approx (0.3 - 0.7)$ fm in comparison with our results. Moreover, the typical time

scale of τ was given by $\tau T = 0.5$, giving $\tau \approx 0.38$ fm at $T \approx 1.45 T_c$ [18]. Interestingly, this time scale is quite compatible with ours. In those LQCD data, it should be noticed that the unrenormalized vector currents for the Kubo formula $\sim \langle J_\mu J_\nu \rangle$ were employed in Refs. [22,42], whereas Ref. [18] made use of the renormalized one. Hence, one may expect systematic errors for σ given in Refs. [22,42]. To estimate those errors is, however, clearly beyond our scope.

In Ref. [19], the quenched SU(2) LQCD was performed, and the electrical conductivity was also estimated as $\sigma = (0.076 \pm 0.010)$ fm^{-1} at $T = 350$ MeV with the transition temperature ~ 313 MeV, taking into account $T = 1.12 T_c$. To be consistent with others using $T_c = 180$ MeV as above, we depict the data point of Ref. [19] at $T = 1.12 \times 180$ MeV ≈ 202 MeV in the left panel of Fig. 2 (diamond), although it was evaluated at $T = 350$ MeV. Being different from other LQCD data, Ref. [19] presented the longitudinal and transverse components of σ separately in the presence of the external magnetic field. Those LQCD data showed that $\sigma_\perp \approx \sigma_\parallel$ beyond T_c for arbitrary values of B_0, whereas $\sigma_\perp \neq \sigma_\parallel$ at $T = 0$ and the difference between them is enhanced by increasing B_0. Qualitatively, this observation of the LQCD results is consistent with ours as indicated by the thick and thin lines in the left panel of Fig. 2. In our calculations, $\sigma_\parallel$ (thin) is smaller than $\sigma_\perp$, mainly because of the negative sign in front of the term $\propto (e_f B_0)^2$ in Eq. (23) in the vicinity of $T \approx 0$. On the contrary, $\sigma_\parallel$ becomes larger than $\sigma_\perp$ at $T = 0$ in Ref. [19].

However, we note that, if we consider the finite number difference between the instanton and anti-instanton numbers, i.e., $\Delta N \equiv N_I - N_{\bar{I}} \neq 0$ [31], which are not taken into account in the present work and correspond to the U$_A$(1) QCD anomaly via the finite chiral quark density related to CME [5–8], the conductivity increases with respect to the external magnetic field. In other words, to observe sizable values for the electrical conductivity enhanced by the external magnetic fields, it is necessary to have the U$_A$(1) QCD anomaly explicitly in the model, in addition to the anomaly-independent terms [31].

Beside the LQCD data, there were several theoretical estimations for the electrical conductivity via effective approaches using the Green-function method [14] and chiral perturbation theory [44]. In Ref. [14], the electrical conductivity was computed for finite temperature and quark density, $T = 100$ MeV and $\mu = 400$ MeV, which

TABLE II. The coefficients $\mathcal{C}_{1,2,3}$ for Eq. (23) for different τ values.

	$\tau = 0.3$ fm	$\tau = 0.5$ fm	$\tau = 0.7$ fm	$\tau = 0.9$ fm
$\mathcal{C}_1$	0.46	0.77	1.08	1.39
$\mathcal{C}_2$ [fm]	4.00×10^{-6}	6.66×10^{-6}	9.33×10^{-6}	1.20×10^{-6}
$\mathcal{C}_3$ [fm^2]	-4.87×10^{-5}	-4.87×10^{-6}	-4.88×10^{-5}	-4.88×10^{-5}

TABLE III.   Typical values of $\mathcal{R}_\gamma$ in Eq. (24) [fm^{-2}] at $B_0 = 0$ for different T and τ values.

	$T = 100$ MeV	$T = 200$ MeV	$T = 300$ MeV	$T = 400$ MeV
$\tau = 0.3$ fm	1.181×10^{-5}	2.700×10^{-5}	5.229×10^{-5}	11.021×10^{-5}
$\tau = 0.5$ fm	2.024×10^{-5}	4.500×10^{-5}	8.940×10^{-5}	18.667×10^{-5}
$\tau = 0.7$ fm	2.811×10^{-5}	6.297×10^{-5}	12.482×10^{-5}	26.089×10^{-5}
$\tau = 0.9$ fm	3.600×10^{-5}	8.100×10^{-5}	16.025×10^{-5}	33.511×10^{-5}

may correspond to the future heavy-ion collision facilities, such as Facility for Antiprotons and Ions Research (FAIR) of Gesellschaft für Schwerionenforschung (GSI) and Nuclotron-based Ion Collider fAcility (NICA) of Joint Institute for Nuclear Research as noted there. By choosing $\tau = 0.9$ fm, it was given that $\sigma \approx 0.04$ fm^{-1}. Note that this value corresponds to $\tau = (0.5–0.7)$ in our results for zero density. In other words, by increasing the quark density, the electrical conductivity decreases at a certain temperature, as expected.

Finally, we would like to estimate the (differential) soft photon ($w_p \rightarrow 0$) emission rate from QGP for the dilepton decay rates, which is related to the electrical conductivity as follows [18,22]:

$$\mathcal{R}_\gamma \equiv \lim_{w_p \rightarrow 0} w_p \frac{dR_\gamma}{d^3|\boldsymbol{p}|} = \frac{3\alpha_{\mathrm{EM}}}{2\pi^2} \sigma T. \qquad (24)$$

The numerical results for $\mathcal{R}_\gamma$ in Eq. (24) are given in the right panel of Fig. 2 for different τ values as in the left panel of Fig. 2. We also depict the other theoretical estimations there, using Eq. (24). It turns out that the value of $\mathcal{R}_\gamma$ increases rapidly in the vicinity of $T = 0$. Beyond that, the slope of $\mathcal{R}_\gamma$ becomes relatively stable with respect to T. Although one can easily have numerical values for $\mathcal{R}_\gamma$ from the numbers given in Table I by multiplying $3\alpha_{\mathrm{EM}}T/(2\pi^2)$, for the convenience of readers, $\mathcal{R}_\gamma$ for some temperatures are listed in Table III.

IV. SUMMARY AND CONCLUSION

We have investigated the electrical conductivity of quark matter at finite temperature and zero quark density ($T \neq 0$, $\mu = 0$), using the dilute instanton-liquid model. The instanton parameters, i.e., the average instanton size and inter-(instanton) distance, were modified as functions of T according to the caloron distribution. Employing the Kubo formula, we computed it in the presence of the external magnetic field in the order of $B_0 \approx m_\pi^2 \times 10$. We compared our results with the LQCD data as well as effective theories. Important observations of the present work are listed as follows:

(i) The electrical conductivity is an increasing function of T and the values for σ depend on the relaxation

time τ of the quark matter. Note that we modify the effective quark mass into a decreasing function of T as well as $|\boldsymbol{k}|$, playing the role of a natural UV regulator and signaling the reduction of the nonperturbative QCD effects at finite T. Typically, we have $\sigma \approx (0.02–0.15)$ fm^{-1} for $T = (0–400)$ MeV with the relaxation time $\tau = (0.3–0.9)$ fm.

(ii) Recent theoretical estimations including the quenched LQCD data are well reproduced for $\tau = (0.3–0.7)$ fm for a wide T range. From the numerical calculations, it turns out that the one order larger σ, estimated in the early LQCD data [22], corresponds to $\tau \approx 5$ fm, which is much larger than other values. This value $\tau \approx 5$ fm is consistent with a conservative estimate of the QGP-medium size.

(iii) The external magnetic field provides only negligible effects on the electrical conductivity even for the very strong one in the order of $B_0 \approx m_\pi^2 \times 10$. However, if we consider the $\mathrm{U}_\mathrm{A}(1)$ anomaly, which is the main source for CME and produced from the number difference between the instanton and anti-instanton in the present theoretical framework, this situation can be altered to a certain extent.

(iv) Using the numerical results obtained, the electrical conductivity is parametrized for $T = (0–400)$ MeV with $\sigma = C_{\mathrm{EM}}(\mathcal{C}_1 T + \mathcal{C}_2 T^2 + \mathcal{C}_3 T^3 + \cdots)$ and, in this parametrization, the coefficients for T^2 and T^3 are almost negligible in comparison to $\mathcal{C}_1$. As a result, we have $\sigma/T \approx (0.46, 0.77, 1.08, 1.39)C_{\mathrm{EM}}$ for $\tau = (0.3, 0.5, 0.7, 0.9)$ fm, respectively. These results are again compatible with other theoretical estimations.

To understand QCD at extreme conditions, the transport coefficients for quark matter are very important physical quantities to be studied. In the present work, we have shown that the instanton model reproduced compatible results for the electrical conductivity with other theoretical calculations including the LQCD data and estimated it as a function of T for different relaxation times of the matter for the first time. Hence, it is quite promising and challenging to investigate other coefficients as well within the same theoretical framework. Other transport coefficients such as the shear and bulk viscosities are under investigation, and related works will appear elsewhere.

[1] S. A. Voloshin, Phys. Rev. C **70**, 057901 (2004).

[2] S. A. Voloshin (STAR Collaboration), Indian J. Phys. B **85**, 1103 (2011).

[3] B. I. Abelev *et al.* (STAR Collaboration), Phys. Rev. C **81**, 054908 (2010).

[4] B. I. Abelev *et al.* (STAR Collaboration), Phys. Rev. Lett. **103**, 251601 (2009).

[5] D. Kharzeev, Phys. Lett. B **633**, 260 (2006).

[6] D. E. Kharzeev, L. D. McLerran, and H. J. Warringa, Nucl. Phys. **A803**, 227 (2008).

[7] P. V. Buividovich, M. N. Chernodub, E. V. Luschevskaya, and M. I. Polikarpov, Phys. Rev. D **80**, 054503 (2009).

[8] K. Fukushima, D. E. Kharzeev, and H. J. Warringa, Phys. Rev. D **78**, 074033 (2008).

[9] D. E. Kharzeev and H. U. Yee, Phys. Rev. D **83**, 085007 (2011).

[10] Y. Burnier, D. E. Kharzeev, J. Liao, and H. U. Yee, Phys. Rev. Lett. **107**, 052303 (2011).

[11] S. i. Nam and C. W. Kao, Phys. Rev. D **83**, 096009 (2011).

[12] G. S. Bali, F. Bruckmann, G. Endrődi, Z. Fodor, S. D. Katz, S. Krieg, A. Schäfer, and K. K. Szabó, J. High Energy Phys. 02 (2012) 044.

[13] D. P. Menezes, M. Benghi Pinto, S. S. Avancini, A. Perez Martinez, and C. Providencia, Phys. Rev. C **79**, 035807 (2009).

[14] B. Kerbikov and M. Andreichikov, arXiv:1206.6044.

[15] A. A. Osipov, B. Hiller, A. H. Blin, and J. da Providencia, Phys. Lett. B **650**, 262 (2007).

[16] B. Hiller, A. A. Osipov, A. H. Blin, and J. da Providencia, SIGMA **4**, 024 (2008).

[17] N. Sadooghi and F. Taghinavaz, Phys. Rev. D **85**, 125035 (2012).

[18] H. T. Ding, A. Francis, O. Kaczmarek, F. Karsch, E. Laermann, and W. Soeldner, Phys. Rev. D **83**, 034504 (2011).

[19] P. V. Buividovich, M. N. Chernodub, D. E. Kharzeev, T. Kalaydzhyan, E. V. Luschevskaya, and M. I. Polikarpov, Phys. Rev. Lett. **105**, 132001 (2010).

[20] F. Karsch, D. Kharzeev, and K. Tuchin, Phys. Lett. B **663**, 217 (2008).

[21] D. J. Evans and G. P. Morriss, *Statistical Mechanics of Non-Equilibrium Liquids* (Academic Press, London, 1990).

[22] S. Gupta, Phys. Lett. B **597**, 57 (2004).

[23] M. Harada and C. Sasaki, Phys. Rev. D **74**, 114006 (2006).

[24] E. V. Shuryak, Nucl. Phys. **B203**, 93 (1982).

[25] D. Diakonov and V. Y. Petrov, Nucl. Phys. **B245**, 259 (1984).

[26] D. Diakonov and A. D. Mirlin, Phys. Lett. B **203**, 299 (1988).

[27] S. i. Nam, J. Phys. G **37**, 075002 (2010).

[28] J. S. Schwinger, Phys. Rev. **82**, 664 (1951).

[29] J. F. Nieves and P. B. Pal, Phys. Rev. D **73**, 105003 (2006).

[30] S. i. Nam, H. Y. Ryu, M. M. Musakhanov, and H.-Ch. Kim, J. Korean Phys. Soc. **55**, 429 (2009).

[31] S. i. Nam, Phys. Rev. D **80**, 114025 (2009).

[32] S. i. Nam and H.-Ch. Kim, Phys. Lett. B **647**, 145 (2007).

[33] T. Schafer and E. V. Shuryak, Rev. Mod. Phys. **70**, 323 (1998).

[34] S. i. Nam and C. W. Kao, Phys. Rev. D **82**, 096001 (2010).

[35] K. Goeke, M. M. Musakhanov, and M. Siddikov, Phys. Rev. D **76**, 076007 (2007).

[36] Y. Maezawa, S. Aoki, S. Ejiri, T. Hatsuda, N. Ishii, K. Kanaya, and N. Ukita, J. Phys. G **34**, S651 (2007).

[37] A. Ali Khan *et al.* (CP-PACS Collaboration), Phys. Rev. D **63**, 034502 (2000).

[38] Y. Aoki, Z. Fodor, S. D. Katz, and K. K. Szabo, Phys. Lett. B **643**, 46 (2006).

[39] Y. Aoki, S. Borsanyi, S. Durr, Z. Fodor, S. D. Katz, S. Krieg, and K. K. Szabo, J. High Energy Phys. 06 (2009) 088.

[40] S. Borsanyi, Z. Fodor, C. Hoelbling, S. D. Katz, S. Krieg, C. Ratti, and K. K. Szabó (Wuppertal-Budapest Collaboration), J. High Energy Phys. 09 (2010) 073.

[41] A. Bazavov *et al.*, Phys. Rev. D **85**, 054503 (2012).

[42] G. Aarts, C. Allton, J. Foley, S. Hands, and S. Kim, Phys. Rev. Lett. **99**, 022002 (2007).

[43] K. Tuchin, Phys. Rev. C **82**, 034904 (2010); **83**, 039903(E) (2011).

[44] D. Fernandez-Fraile and A. Gomez Nicola, Eur. Phys. J. C **62**, 37 (2009).